# Using snowflake surface area-to-volume ratio to model and interpret snowfall triple-frequency radar signatures

Mathias Gergely[1], Steven J. Cooper[1], and Timothy J. Garrett[1]

[1]Department of Atmospheric Sciences, University of Utah, 135 S 1460 E Room 819, Salt Lake City, UT 84112, USA.

*Correspondence to:* Mathias Gergely (mathias.gergely@utah.edu)

**Abstract.** The snowflake microstructure determines the microwave scattering properties of individual snowflakes and has a strong impact on snowfall radar signatures. In this study, the microstructure of individual snowflakes is approximated by collections of randomly distributed ice spheres where the size and number of the constituent ice spheres are specified by the snowflake mass and ice surface area-to-volume ratio (SAV) and the bounding volume is given by the snowflake maximum dimension.

5  Radar backscatter cross sections for the ice sphere collections are calculated at X-, Ku-, Ka-, and W-band frequencies and then used to model snowfall triple-frequency radar signatures for exponential snowflake size distributions (SSDs). Additionally, first results are presented for using snowflake complexity values derived from high-resolution multi-view snowflake images as indicator of snowflake SAV. The modeled snowfall triple-frequency radar signatures cover a wide range of triple-frequency signatures that were previously determined from radar reflectivity measurements and illustrate characteristic differences related

10 to snow type, quantified through snowflake SAV, and snowflake size. The results show high sensitivity to snowflake SAV and SSD maximum size but are less affected by uncertainties in the parameterization of snowflake mass, indicating the importance of a realistic description of snowflake SAV for a quantitative interpretation of snowfall triple-frequency radar signatures.

## 1 Introduction

Snowfall retrievals from radar remote sensing of snow clouds are highly sensitive to the applied characterization of the

15 snowflake microstructure, i.e., of snowflake mass and shape (e.g., Matrosov, 2007; Liu, 2008; Kulie et al., 2010). In previous studies that have analyzed snowfall microwave scattering signatures, snowflakes have often been approximated by (i) mixed ice-air spheres or spheroids parameterized with respect to snowflake size and aspect ratio (e.g., Matrosov, 1992; Hogan et al., 2006, 2012) or by (ii) detailed three-dimensional (3D) shape models of single snow crystals or aggregate snowflakes based on various idealized ice crystals like bullet rosettes, dendrites, plates, or needles (e.g., Kulie and Bennartz, 2009; Nowell et al.,

20 2013; Ori et al., 2014; Honeyager et al., 2016). This study instead uses ice surface area-to-volume ratio to characterize the snowflake microstructure and model snowfall triple-frequency radar signatures.

In recent years, several studies have found that the 'soft' spheroidal particle model, where the volume, density, and complex index of refraction of a homogeneously mixed ice-air spheroid are derived from the snowflake size, mass, and aspect ratio, only yields a realistic description of microwave backscatter for small snowflakes and at low frequencies (e.g., Petty and Huang,

25 2010; Tyynelä et al., 2011; Nowell et al., 2013). Furthermore, the analysis of radar reflectivity measurements collected simul-

Atmospheric
Chemistry
and Physics
Discussions

taneously at three microwave frequency bands has shown that the range of observed snowfall triple-frequency radar signatures is much larger than the total range of modeled snowfall radar signatures when approximating snowflakes as soft spheroids; especially triple-frequency radar signatures of snowfall characterized by large aggregate snowflakes fall outside the modeled range (Leinonen et al., 2012; Kulie et al., 2014; Kneifel et al., 2015). Using detailed 3D shape models instead of soft spheroids

5    to approximate snowflakes leads to a wider range of modeled snowfall triple-frequency radar signatures and indicates better agreement between observed and modeled snowfall radar signatures.

Due to the large variety of (visually distinct) snow types, defined by characteristic geometric shapes resembling the snowflake microstructure, such as planar dendrites or aggregates of plates (Magono and Lee, 1966; Kikuchi et al., 2013; Fontaine et al., 2014), and the high natural variability of snowflake microstructural properties like size and aspect ratio (e.g., Brandes et al.,

10    2007; Gergely and Garrett, 2016), modeling microwave backscatter in snowfall based on detailed snowflake 3D shape models requires significant computational resources and time, e.g., when determining backscatter cross sections for a large number of snowflake models with the widely used discrete dipole approximation (Draine and Flatau, 1994). Therefore, it would be desirable to identify effective microstructural parameters that quantify snowflake shape independent of snow type and still explain important features of observed and modeled snowfall radar signatures, thus further constraining snowflake shape for

15    snowfall remote sensing.

In materials science, four basic characteristics play a central role for an objective and quantitative description of 3D microstructures: volume fraction or equivalently (mass) density, surface area per volume, integrated mean curvature per volume, and integrated Gaussian curvature per volume (Ohser and Mücklich, 2000). Physical and chemical properties strongly depend on these characteristics and can often already be analyzed faithfully when the 3D microstructure is quantified through all or

20    some of these four characteristics. A realistic description of ice volume fraction or snow density and of the ratio of ice surface area to volume is crucial for modeling light scattering and radiative transfer at optical wavelengths in falling and deposited snow, for example (Grenfell and Warren, 1999; Grenfell et al., 2005; Kokhanovsky and Zege, 2004; Picard et al., 2009). Besides snowflake density, however, none of these four basic characteristics have been investigated to evaluate the impact of snowflake shape on snowfall microwave scattering signatures.

25    In this study, snowflake density and ice surface area-to-volume ratio (SAV) are used to model snowflake backscatter cross sections at X-, Ku-, Ka-, and W-band frequencies and then derive snowfall triple-frequency radar signatures for realistic snowflake size distributions. The impact of snowflake SAV on snowfall triple-frequency radar signatures is analyzed based on high-resolution snowflake imaging data collected with the Multi-Angle Snowflake Camera (MASC; Garrett et al., 2012), a pre-established relation by Heymsfield et al. (2004) for deriving snowflake mass from snowflake maximum dimension, and the

30    snowflake SAV range given by Honeyager et al. (2014).

First, MASC measurements are presented in Sect. 2. The applied methodology for modeling snowflake backscatter cross sections and snowfall triple-frequency radar signatures is described in Sect. 3. Individual snowflakes are approximated by collections of solid ice spheres where the size and number of all constituent ice spheres are specified by the snowflake mass and SAV and the bounding volume is defined by the snowflake maximum dimension. Backscatter cross sections of these

35    collections of ice spheres are calculated with the generalized multiparticle Mie solution (Xu, 1995; Xu and Å. S. Gustafson,

Atmospheric
Chemistry
and Physics
Discussions

2001). For the same snowflake mass, different SAV values lead to collections of ice spheres characterized by a different ice sphere size and number. This characteristic forms the basis for analyzing the impact of snowflake SAV on modeled snowflake backscatter cross sections and snowfall triple-frequency radar signatures in Sect. 4. The analysis includes a comparison with snowfall triple-frequency radar signatures that are determined for soft spheroids and for snowflakes modeled according to the

5 self-similar Rayleigh–Gans approximation (Hogan and Westbrook, 2014; Hogan et al., 2017). Additionally, Sect. 4 shows first results for using snowflake complexity values derived from MASC images as indicator of snowflake SAV. Modeled snowfall triple-frequency radar signatures are discussed in the context of observed and modeled snowfall radar signatures that were presented in previous studies. Section 5 summarizes important results and conclusions.

## 2    Snowflake observations

10 First, the Multi-Angle Snowflake Camera (MASC) and the derived snowflake microstructural properties are described briefly (a more detailed description was given by Garrett et al., 2012). As the applied approach for modeling the impact of snowflake SAV on snowfall radar signatures is partially based on collected snowflake data, MASC measurement results are also presented before the modeling method is detailed in Sect. 3.

### 2.1    Measurement method

15 Snowflake microstructural properties are obtained from MASC photographs that were captured at Alta (UT, USA) and at Barrow (AK, USA) during winter 2014. The MASC provides multi-view snowflake images from three cameras that are separated by $36°$ and point at an identical focal point at a distance of 10 cm. The cameras and three light-emitting diodes serving as flash lights are triggered simultaneously when a snowflake falls through an array of near-infrared emitter–detector pairs sampling the horizontal field of view. Snowflakes with maximum dimensions of about 0.2 mm and larger are recorded at a resolution of

20 about 30 μm and identified in the images using a Sobel edge detection algorithm. Figure 1 shows images of two snowflakes captured by the MASC center camera at Alta.

In this study, MASC images are used to derive the snowflake diameter $D$ or maximum dimension along the snowflake major axis, the orientation angle $\theta$ of the snowflake major axis with respect to the horizontal plane, and the snowflake complexity $\chi$ defined as the ratio of the snowflake perimeter to the circumference of a circle with the same area as the snowflake projection

25 image (illustrated in Fig. 1). For all snowflakes, $D$, $\theta$, and $\chi$ are given as average values determined from the MASC single-view images of the snowflakes.

The applied definition of $\chi$ quantifies snowflake complexity based on the boundary curve length of two-dimensional (2D) snowflake images. Projection images of spherical particles are characterized by a circular boundary curve independent of viewing direction, and thus by a complexity of $\chi = 1$. As a circle has the shortest perimeter of any boundary curve for a given

30 enclosed area, all non-spherical particle shapes lead to complexity values of $\chi > 1$. Accordingly, heavily rimed graupel snow is described by a low snowflake complexity of $\chi \approx 1$ and large aggregate snowflakes are characterized by higher complexity values (see examples in Fig. 1). This 2D description of snowflake complexity is chosen because it corresponds conceptually

Atmospheric
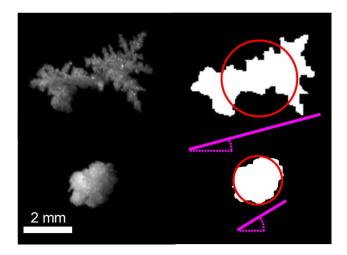Chemistry
and Physics
Discussions



**Figure 1.** (left) MASC single-view images of two snowflakes: (top) aggregate snowflake and (bottom) heavily rimed graupel snow. (right) Illustration of the corresponding projection images of perimeter $P$ (highlighted white regions) and area-equivalent circles of circumference $C$ (outlined in red), leading to complexity values $\chi = \frac{P}{C}$ of (top) $\chi = 2.1$, (bottom) $\chi = 1.2$. Snowflake diameters $D$ and orientation angles $\theta$ are indicated by solid and dotted magenta lines, respectively: (top) $D = 5.7$ mm, $\theta = 16°$; (bottom) $D = 2.3$ mm, $\theta = 31°$.

to characterizing the complexity of snowflake 3D microstructures based on their boundary surface area (used for modeling snowflake backscatter cross sections in Sect. 3.2). The definition of $\chi$ in this study therefore differs from the definition of snowflake complexity introduced by Garrett and Yuter (2014), which additionally included brightness variations within each MASC image.

One MASC was installed at Alta Ski Resort at 2590 m above sea level (a.s.l) in Collins Gulch within the Wasatch Mountain Range. A second MASC was located at Barrow at the North Slope of Alaska Atmospheric Radiation Measurement (ARM) site at 10 m a.s.l., approximately 500 km north of the Arctic Circle on the coast of the Arctic Ocean.

## 2.2 Measurement results

Figure 2 shows the distributions of snowflake diameter $D$, complexity $\chi$, and orientation angle $\theta$ derived from all qualifying MASC observations with realistic complexity values of $\chi \geq 1$ that were collected at Alta and at Barrow during winter 2014, resulting in a MASC data set of $4.4 \cdot 10^5$ sampled snowflakes. Snowflake size distributions $N(D)$ are expressed as frequency size distributions and reflect the number of snowflakes sampled at Alta ($4.3 \cdot 10^5$) and at Barrow ($10^4$). For snowflake complexity and orientation, the presented relative distributions are normalized with respect to the maximum values $N_{\max}(\chi)$ and $N_{\max}(\theta)$ of the respective frequency distributions $N(\chi)$ and $N(\theta)$.

The distributions of snowflake diameters and complexities in Fig. 2 are dominated by small values and show exponential decay for diameters of $D \gtrsim 1$ mm and for the entire complexity range of $\chi \geq 1$. In contrast to snowflake diameters and complexities, snowflake orientation angles are characterized by a nearly uniform distribution with mean values of $\overline{\theta} = 40°$ derived for the set of MASC observations at Alta and $\overline{\theta} = 45°$ at Barrow.
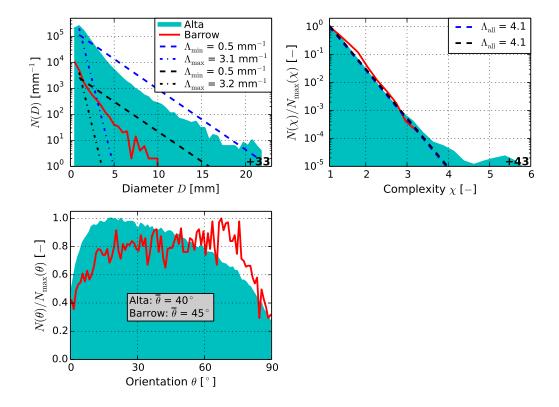
Atmospheric
Chemistry
and Physics
Discussions



**Figure 2.** Snowflake (frequency) size distributions $N(D)$ and relative distributions of snowflake complexity $\chi$ and orientation $\theta$ for $4.4 \cdot 10^5$ snowflakes sampled by MASC at Alta and Barrow. Dashed lines represent (top left) minimum and maximum slope parameters $\Lambda_{\min}$ and $\Lambda_{\max}$ of exponential snowflake size distributions $N(D)$ fitted to 47 snowstorms at Alta and to 7 snowstorms at Barrow following Eq. (1) and (top right) slope parameters $\Lambda_{\text{all}}$ of exponential complexity distributions $N(\chi)$ fitted to combined snowflake data at Alta and at Barrow. Numbers in bottom right corners indicate extreme values of $D$ and $\chi$ outside the plotted range. Mean orientation angles at Alta and at Barrow are indicated by $\overline{\theta}$.

Similar to previous studies that have used exponential snowflake size distributions to describe snowfall (e.g., Matrosov, 2007; Kneifel et al., 2011), snowflake (frequency) size distributions $N(D)$ [mm$^{-1}$] in this study are expressed through

$$N(D) = N_0 \exp(-\Lambda D) , \qquad (1)$$

where $\Lambda$ is the exponential slope parameter specifying the width of the distribution and $N_0$ [mm$^{-1}$] denotes the scaling
5  factor determined by the overall snowflake sample size. Commonly, $N(D)$ and $N_0$ are additionally normalized with respect to atmospheric volume to account for the atmospheric snow water content, giving $N(D)$ and $N_0$ in units of mm$^{-1}$ m$^{-3}$. As the normalization of $N(D)$ has no impact on the analyzed dual-wavelength ratios of modeled $Z_e$ in Sect. 4.2, the scaling factor $N_0$ is ignored in the analysis and exponential distributions are only specified through the exponential slope parameter $\Lambda$.

Exponential snowflake size distributions $N(D)$ were fitted to MASC data restricted to $D > 1$ mm and collected for 47 snowstorms at Alta and for 7 snowstorms at Barrow with snowfall periods between 4 and 24 h. A similar total range and mean value of $\Lambda$ is found for both sets of MASC data (see Fig. 2). At Alta, $N(D)$ for individual snowstorms are characterized by values of $\Lambda_{min} = 0.5$ mm$^{-1} \leq \Lambda \leq \Lambda_{max} = 3.1$ mm$^{-1}$ with mean $\overline{\Lambda} = 1.2$ mm$^{-1}$. At Barrow, the range of $N(D)$ is given by $0.5$ mm$^{-1} \leq \Lambda \leq 3.2$ mm$^{-1}$ with mean $\overline{\Lambda} = 1.4$ mm$^{-1}$. The range of the derived exponential slope parameters indicates snowflake size distributions $N(D)$ that are similar to previously presented snowflake size distributions using different measurement methods (e.g., Brandes et al., 2007; Tiira et al., 2016, with reported median volume diameters $D_0$ of the derived snowflake size distributions converted to $\Lambda = 3.67/D_0$ for $N(D)$ given by Eq. (1)).

Exponential snowflake complexity distributions $N(\chi) = N_1 \exp(-\Lambda_{all}\chi)$ were also fitted to the MASC data collected at Alta and at Barrow. Here, all data at each location were combined into a single data set. The derived snowflake complexity distributions both at Alta and at Barrow are characterized by an exponential slope parameter of $\Lambda_{all} = 4.1$ (see Fig. 2).

To illustrate the correlation between snowflake diameter $D$ and complexity $\chi$, Fig. 3 shows a logarithmic 2D histogram of the frequency distributions for $D$ and $\chi$ at Alta and Barrow (Fig. S1 in the Supplement shows the corresponding non-logarithmic 2D histogram). Derived mean complexity values $\overline{\chi}$ per size bin $\Delta D$ are shown separately for both MASC data sets collected at Alta ($\overline{\chi}/\Delta D$ given for $D \leq 15$ mm) and at Barrow ($\overline{\chi}/\Delta D$ given for $D \leq 10$ mm). As already seen in Fig. 2, small values of $D$ and $\chi$ dominate the distributions. Additionally, mean complexity $\overline{\chi}$ generally increases with increasing snowflake diameter. Notably, snowflake complexities of $\chi = 1.0$ are not observed for snowflake diameters of $D \gtrsim 3$ mm. These results are in line with previous observations suggesting that larger snowflakes are generally aggregates characterized by a high complexity of the snowflake microstructure (Garrett and Yuter, 2014).

Based on the mean snowflake complexity values $\overline{\chi}$ per size bin $\Delta D$ shown in Fig. 3, a snowflake complexity-to-diameter relation is then defined by a modified power law as

$$\chi(D) = 1 + aD^b ,\tag{2}$$

with parameters $a$ and $b$. Power laws have been applied to parameterize a variety of snowflake properties $y$ with respect to snowflake size, illustrated by the density-diameter relation in Eq. (3), for example. In Eq. (2), the constant of $\chi_0 = 1$ is added to the commonly used pure power law of the form $y(D) = aD^b$ due to the definition of $\chi$, which leads to a minimum value of $\chi_{min}(D) = \chi_0 = 1$ (see Sect. 2.1).

Figure 3 shows the two curves obtained by the least-squares method for fitting Eq. (2) to the mean complexity values $\overline{\chi}$ per size bin $\Delta D$ that were determined for the MASC data recorded at Alta and at Barrow. These two $\chi(D)$ relations, specified through parameters of $a = 0.20, b = 0.75$ at Alta and $a = 0.36, b = 0.54$ at Barrow, are dominated by the power-law term of $aD^b$ for large snowflakes and thus follow the observed increase in $\chi$ with increasing snowflake diameter, but also reflect the observed convergence of $\chi \to 1$ for small snowflakes.
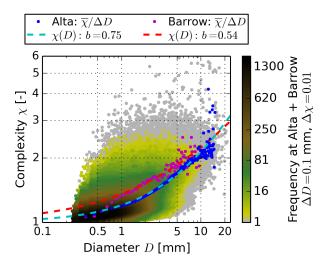
**Figure 3.** Logarithmic 2D histogram for all MASC data of snowflake diameter $D$ and complexity $\chi$ presented in Fig. 2, with bin sizes of $\Delta D = 0.1$ mm and $\Delta \chi = 0.01$. Mean complexity values per size bin are indicated by $\overline{\chi}/\Delta D$ for snowflake data recorded at Alta and at Barrow separately. Snowflake complexity-to-diameter relations $\chi(D)$ for the data sets collected at Alta and at Barrow are determined by the least-squares method for fitting Eq. (2) to the values of $\overline{\chi}/\Delta D$ and characterized by the power-law exponent $b$.

## 3 Modeling method

Snowflake backscatter cross sections and snowfall radar reflectivity factors are modeled at X-, Ku-, Ka-, and W-band frequencies of 10, 14, 35, and 94 GHz, respectively. Snowfall triple-frequency radar signatures are then defined by the two dual-wavelength ratios (DWRs) of modeled snowfall radar reflectivity factors at (i) Ka and W band and at (ii) either X and Ka band or Ku and Ka band, indicated as DWR Ka/W, DWR X/Ka, and DWR Ku/Ka, respectively. The selected frequencies are within ±1 GHz of X-, Ku-, Ka-, and W-band frequencies commonly used for the analysis of snowfall triple-frequency radar signatures (e.g., Leinonen et al., 2012; Kulie et al., 2014; Kneifel et al., 2015, 2016; Yin et al., 2017).

### 3.1 Snowflake mass

No coincident measurements of snowflake mass are available for the analyzed MASC data in Sect. 2. Therefore, snowflake mass is derived from measured snowflake diameter $D$ following a previously determined density-diameter relation that uses a similar definition of snowflake diameter (Heymsfield et al., 2004, abbreviated as H04 throughout the text). H04 determined effective ice-cloud particle densities by combining observations by airborne 2D optical array probes with coincident measurements of cloud ice water content. According to their results, snowflake density $\rho_{\mathrm{f}}$ [g cm$^{-3}$] and mass $m_{\mathrm{f}}$ [mg] are calculated from snowflake maximum dimension $D$ [mm] for a spherical snowflake bounding volume $V_{\mathrm{f}}$ of diameter $D$:

$$\rho_{\mathrm{f}}(D) = 0.104 D^{-0.950} \tag{3}$$

and

$$m_{\mathrm{f}}(D) = \rho_{\mathrm{f}}(D)V_{\mathrm{f}} = \frac{\pi}{6}\rho_{\mathrm{f}}(D)D^3 . \tag{4}$$

Here, derived $\rho_{\mathrm{f}}(D)$ values are limited to the density of pure ice $\rho_{\mathrm{ice}} = 0.917\,\mathrm{g\,cm^{-3}}$, leading to densities of $\rho_{\mathrm{f}}(D) = \rho_{\mathrm{ice}}$ for snowflakes with $D \leq 0.1\,\mathrm{mm}$.

5    With Eqs. (3) and (4), snowflake mass $m_{\mathrm{f}}$ can alternatively be expressed through the radius $r_{\mathrm{eq}}$ of a single mass-equivalent ice sphere given by

$$r_{\mathrm{eq}}^3(D) = \frac{3m_{\mathrm{f}}(D)}{4\pi\rho_{\mathrm{ice}}} . \tag{5}$$

Analyzed snowflake and snowfall backscatter properties in Sect. 4 are determined from different modeling approaches that all rely on the same parameterization of snowflake mass following Eqs. (3)–(5). The impact of the parameterization of snowflake

10    mass on the presented results and conclusions is evaluated by comparing modeling results that are derived for modifying all snowflake densities $\rho_{\mathrm{f}}(D)$ obtained from Eq. 3 by $\pm 25\,\%$ and by $\pm 50\,\%$.

### 3.2    Modeling snowflake backscatter cross sections based on surface area-to-volume ratio

In this study, microwave backscatter by a snowflake is modeled by calculating the (radar) backscatter cross section $\sigma_{\mathrm{b}}$ for snowflake mass- and SAV-equivalent collections of non-overlapping ice spheres with the generalized multiparticle Mie (GMM)

15    solution (Xu, 1995; Xu and Å. S. Gustafson, 2001). Calculated $\sigma_{\mathrm{b}}$ values correspond to the differential scattering cross sections at backscatter multiplied by $4\pi$ (see Bohren and Huffman (1983) for a discussion on commonly applied conventions for expressing backscatter by a particle). The modeling approach is outlined in Fig. 4 and described in this section.

Snowflakes are specified by the snowflake diameter $D$, the snowflake mass $m_{\mathrm{f}}$ derived from $D$ according to Eqs. (3) and (4), and by the normalized snowflake surface area-to-volume ratio $\xi$ defined as the ratio of snowflake ice surface area-to-volume

20    ratio $\mathsf{SAV}_{\mathrm{f}}$ to the surface area-to-volume ratio $\mathsf{SAV}_{\mathrm{s}}$ of a mass-equivalent ice sphere:

$$\xi = \frac{\mathsf{SAV}_{\mathrm{f}}}{\mathsf{SAV}_{\mathrm{s}}} . \tag{6}$$

For a given ice volume or snowflake mass, spherical ice particles have the smallest surface area of any snowflake 3D microstructure and a surface area-to-volume ratio of $\mathsf{SAV}_{\mathrm{f}} = \mathsf{SAV}_{\mathrm{s}} = 6/D = 3/r$. Therefore, a normalized SAV of $\xi = 1$ corresponds with a solid ice sphere, and all other snowflake shapes are characterized by normalized SAV values of $\xi > 1$. Similar to the defi-

25    nition of snowflake complexity $\chi$ derived from snowflake images in Sect. 2, increasing values of $\xi$ imply a more significant deviation of the snowflake shape from a mass-equivalent ice sphere, and thus an increasing complexity of the snowflake 3D microstructure. Heavily rimed graupel snow is then described by low normalized surface area-to-volume ratios of $\xi \approx 1$ and large unrimed aggregate snowflakes are characterized by higher values of $\xi$, for example.

The variability in snowflake SAV is derived from the total range of $\xi$ values determined by Honeyager et al. (2014). They

30    used a Voronoi cell-based approach to define an effective SAV by Eq. (6) for their database of detailed 3D shape models and found values of $1 \leq \xi \leq 5$.
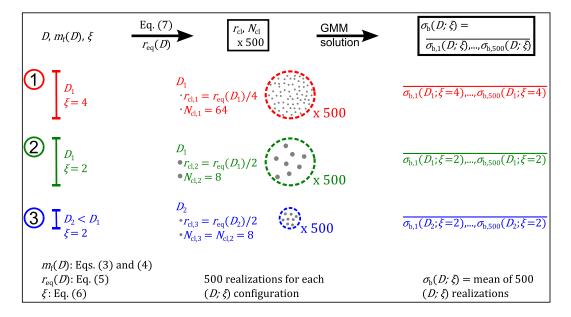
**Figure 4.** Sketch of the modeling approach described in Sect. 3.2, with three examples highlighted in red, green, and blue. The impact of normalized snowflake surface area-to-volume ratios of $1 \leq \xi \leq 5$ on modeled snowflake backscatter cross sections $\sigma_{\mathrm{b}}$ is investigated by applying the generalized multiparticle Mie (GMM) solution to collections of randomly distributed ice spheres characterized by the radius $r_{\mathrm{cl}}$ and the number $N_{\mathrm{cl}}$ of the constituent ice spheres and by the snowflake diameter $D$ indicating the bounding volume of the ice sphere collections.

A snowflake defined by the three values of $D$, $m_{\mathrm{f}}(D)$, and $\xi$ is approximated as a collection of ice spheres, where the radius $r_{\mathrm{cl}}$ and the number $N_{\mathrm{cl}}$ of the constituent ice spheres are specified by $m_{\mathrm{f}}$, or equivalently by $r_{\mathrm{eq}}$ through Eq. (5), and by $\xi$:

$$r_{\mathrm{cl}}(r_{\mathrm{eq}}, \xi) = \frac{r_{\mathrm{eq}}}{\xi} \,,$$

5 $$N_{\mathrm{cl}}(\xi) = \xi^3 \,. \tag{7}$$

Equation (7) preserves snowflake mass and normalized surface area-to-volume ratio given by $m_{\mathrm{f}} = \frac{4\pi}{3} \rho_{\mathrm{ice}} r_{\mathrm{eq}}^3 = \frac{4\pi}{3} \rho_{\mathrm{ice}} N_{\mathrm{cl}} r_{\mathrm{cl}}^3$ and $\xi = \mathrm{SAV}_{\mathrm{f}}/\mathrm{SAV}_{\mathrm{s}} = (\frac{3}{r_{\mathrm{cl}}})/(\frac{3}{r_{\mathrm{eq}}})$, respectively. The snowflake diameter $D$ specifies the bounding volume $V_{\mathrm{f}}$ of the collection of ice spheres according to Eq. (4).

The MASC observations presented in Sect. 2.2 showed nearly uniform distributions of snowflake orientation angles and 10 therefore suggest randomly oriented snowflakes for the analyzed snowfall data. To account for random snowflake orientation in the applied modeling approach and also include a variety of 3D microstructures derived for the same values of $D$, $m_{\mathrm{f}}(D)$, and $\xi$, 500 realizations of randomly distributed non-overlapping ice spheres inside $V_{\mathrm{f}}$ are used to model each configuration of $D$ and $\xi$, or equivalently each configuration of $r_{\mathrm{cl}}$ and $N_{\mathrm{cl}}$. The snowflake backscatter cross section $\sigma_{\mathrm{b}}(D; \xi)$ is then determined as the mean of all backscatter cross sections $\sigma_{\mathrm{b,1}}(D; \xi), ..., \sigma_{\mathrm{b,500}}(D; \xi)$ that are calculated by the GMM solution for the 500

individual realizations. Here, the refractive index of all constituent ice spheres is given by the complex refractive index $n_{\mathrm{ice},\lambda}$ of pure ice calculated according to Mätzler and Wegmüller (1987), leading to refractive indices of $n_{\mathrm{ice},\lambda} = 1.8 + 2.3 \cdot 10^{-4}i$, $1.8 + 3.2 \cdot 10^{-4}i$, $1.8 + 8.2 \cdot 10^{-4}i$, and $1.8 + 2.4 \cdot 10^{-3}i$ at 10, 14, 35, and 94 GHz, respectively.

Sets of 500 realizations were chosen for averaging because mean values of $\sigma_{\mathrm{b}}(D;\xi)$ stabilize to within relative differences of $\Delta\sigma_{\mathrm{b}}/\sigma_{\mathrm{b}} < 0.1$ once $10^1$ to $10^2$ collections of randomly distributed ice spheres are included (see Fig. S2 in the Supplement). These uncertainties in $\sigma_{\mathrm{b}}(D;\xi)$ are small compared to the impact of $\xi$ on modeled $\sigma_{\mathrm{b}}(D;\xi)$, characterized by relative differences of up to $\Delta\sigma_{\mathrm{b}}/\sigma_{\mathrm{b}} > 10^2$ in Sect. 4.1. The applied methodology then quantifies the impact of SAV on the modeled snowflake backscatter cross sections without including effects due to the spatial distribution or clustering of the number of $N_{\mathrm{cl}}$ ice spheres inside the bounding volume $V_{\mathrm{f}}$.

To analyze the impact of snowflake surface area-to-volume ratio on modeled backscatter cross sections for a given snowflake diameter $D$, $\sigma_{\mathrm{b}}(D;\xi)$ are calculated for seven values of $N_{\mathrm{cl}} = 1$, 4, 8, 16, 27, 64, and 125, corresponding to normalized snowflake surface area-to-volume ratios of $\xi = 1.0$, 1.6, 2.0, 2.5, 3.0, 4.0, and 5.0, respectively. Backscatter cross sections for intermediate $N_{\mathrm{cl}}$ or $\xi$ values are determined from linear interpolations of the seven calculated $\sigma_{\mathrm{b}}(D;\xi)$ values. The parameter $\xi$, describing the snowflake microstructure, and the number $N_{\mathrm{cl}}$, specifying the corresponding collections of randomly distributed ice spheres inside the snowflake bounding volume, are used interchangeably throughout this study according to Eq. (7).

For comparison, the analysis also includes snowflake approximations as mass-equivalent soft (mixed ice-air) oblate spheroids and snowflakes modeled according to the self-similar Rayleigh–Gans approximation (SSRGA; Hogan and Westbrook, 2014; Hogan et al., 2017). Backscatter cross sections of randomly oriented soft spheroids are calculated with the T-matrix method (Waterman, 1971), using the implementation of Mishchenko and Travis (1998) within the PyTMatrix software package of Leinonen (2014). Aspect ratios of $\alpha = 1$, 0.6, and 0.2 are considered, representing soft spheres with $\alpha = 1$, spheroids that are characterized by typical average values of $\alpha = 0.6$ found in snowflake observations (e.g., Korolev and Isaac, 2003; Gergely and Garrett, 2016) and used for the interpretation of snow- and ice-cloud radar measurements (Matrosov et al., 2005; Hogan et al., 2012), and spheroids described by extreme values of observed snowflake aspect ratios of $\alpha = 0.2$. Refractive indices of the soft spheroids are determined by applying the Maxwell–Garnett mixing rule (Maxwell Garnett, 1904) for volume mixtures of ice inclusions in air, given by the mass $m_{\mathrm{f}}$ and the volume $\alpha V_{\mathrm{f}}$ of the spheroidal snowflakes, and for the complex refractive index $n_{\mathrm{ice},\lambda}$ of pure ice. The SSRGA has been derived to approximate backscatter cross sections for detailed 3D shape models of aggregate snowflakes based on a statistical description of mean snowflake microstructure and deviation from the mean microstructure. Calculated $\sigma_{\mathrm{b}}$ values with the SSRGA represent ensemble averages for $10^1$ different realizations of the snowflake 3D microstructure with the same snowflake diameter $D$, for 50 random orientations of each snowflake 3D shape model, and for then illuminating each of the reoriented 3D shape models along its three orthogonal directions. Here, the SSRGA is applied to snowflake masses derived by Eqs. (3) and (4) and for complex refractive indices $n_{\mathrm{ice},\lambda}$ of pure ice, using the parameterizations listed by Hogan et al. (2017) for aggregate snowflakes that were generated according to Westbrook et al. (2004), abbreviated as 'W04' throughout the text, and according to Nowell et al. (2013), referred to as 'N13'.

## 3.3 Snowfall triple-frequency radar signatures

To derive snowfall triple-frequency radar signatures at (i) X, Ka, and W band and at (ii) Ku, Ka, and W band, snowflake (radar) backscatter cross sections $\sigma_b$ modeled according to Sect. 3.2 are integrated for exponential snowflake size distributions $N(D)$ expressed through Eq. (1), yielding the corresponding snowfall (equivalent) radar reflectivity factors $Z_e$ (e.g., Matrosov, 2007; Liu, 2008):

$$Z_e = \frac{\lambda^4}{\pi^5} \left| \frac{n_{w,\lambda}^2 + 2}{n_{w,\lambda}^2 - 1} \right|^2 \int_0^{D_{\max}} \sigma_b(D; \xi) N(D) dD , \tag{8}$$

where $n_{w,\lambda}$ refers to the complex refractive index of liquid water at wavelengths of $\lambda = 30.0,\ 21.4,\ 8.6$ and $3.2$ mm for the analyzed frequencies of 10, 14, 35, and 94 GHz, respectively. Here, $n_{w,\lambda}$ is determined for pure water at a temperature of $0\,^\circ\text{C}$ following Meissner and Wentz (2004).

Snowfall triple-frequency radar signatures are then given by dual-wavelength ratios (DWRs, Kneifel et al., 2011) of

$$\text{DWR } \lambda_1/\lambda_2 = 10 \cdot \log_{10}\left( \frac{Z_{e,\lambda_1}}{Z_{e,\lambda_2}} \right) = \text{dBZ}_{e,\lambda_1} - \text{dBZ}_{e,\lambda_2}\ [\text{dB}] , \tag{9}$$

where $\lambda_1/\lambda_2$ indicate the pairs of analyzed radar frequency bands of X/Ka, Ku/Ka, and Ka/W.

Radar reflectivity factors $Z_e$ are calculated by Eq. (8) for snowflake diameters of $D \leq D_{\max} = 23.6$ mm, or for mass-equivalent ice sphere radii of $r_{eq} \leq 2.1$ mm according to Eqs. (3)–(5). This size range covers more than 99.99 % of all snowflakes that were observed with the MASC in Sect. 2.2. Snowflake size distributions $N(D)$ given by Eq. (1) with exponential slope parameters of $0.3 \leq \Lambda \leq 5.0$ mm$^{-1}$ are included in the analysis. This range of $\Lambda$ covers all $N(D)$ determined from the MASC measurements presented in Sect. 2.2, corresponds with size distributions derived from snowflake observational data that were collected with different measurement methods (e.g., Brandes et al., 2007; Tiira et al., 2016), and is similar to $\Lambda$ ranges used in prior studies that have analyzed snowfall triple-frequency radar signatures (Kneifel et al., 2011; Leinonen et al., 2012).

In Sect. 4.2, snowfall triple-frequency radar signatures are also modeled for size distributions limited to snowflake diameters of $D \leq 10.0$ mm and $D \leq 5.0$ mm. The corresponding triple-frequency radar signatures are determined by applying the described modeling approach in this section for modified snowflake maximum diameters of $D_{\max} = 10.0$ mm and $D_{\max} = 5.0$ mm.

The study analyzes the impact of snowflake surface area-to-volume ratio (SAV) on snowfall radar signatures based on synthetically generated expressions $\xi(D)$ that relate normalized SAV to snowflake diameter with $1 \leq \xi(D) \leq 5$ for $0 \leq D \leq D_{\max}$. Based on the MASC observations in Sect. 2.2 where the average snowflake complexity $\chi(D)$ for all recorded snowflakes with maximum dimension $D$ was derived from 2D images and expressed through a power law plus constant of one in Eq. (2), $\xi(D)$ relations indicating the complexity of the snowflake 3D microstructure are again formulated as modified power laws of

$$\xi(D) = 1 + pD^q . \tag{10}$$

Figure 5 shows several $\xi(D)$ curves that illustrate the total range of power-law exponents $q$ considered in the analysis, including constant values that are determined by setting $q = 0$. The parameter $p$ is merely a scaling factor confining Eq. (10) to the
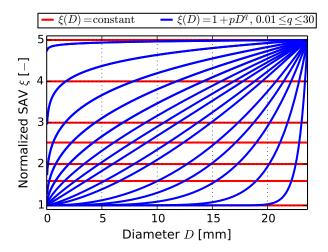
**Figure 5.** Synthetically generated $\xi(D)$ relations for deriving snowflake normalized surface area-to-volume ratio (SAV) from snowflake diameter by Eq. (10) with $D \leq D_{\max} = 23.6$ mm. Shown $\xi(D)$ curves reflect the total range of $\xi(D)$ relations used for modeling snowfall triple-frequency radar signatures in Sect. 4.2.

interval of $1 \leq \xi(D) \leq 5$. Here, only monotonically increasing $\xi(D)$ with $q \geq 0$ are considered because the analyzed MASC observations in Sect. 2.2 indicated an increase in snowflake complexity with increasing snowflake size.

Constant $\xi(D) = 1.0, 1.6, 2.0, 2.5, 3.0, 4.0$, and $5.0$ shown in Fig. 5 are used to model snowflake backscatter cross sections in Sect. 4.1 and lead to a wide range of characteristic snowfall triple-frequency radar signatures in Sect. 4.2. The discussion of how snowflake surface area-to-volume ratio affects modeled snowfall triple-frequency radar signatures in Sect. 4.2 focuses on these seven constant $\xi(D)$ relations. Modified power-law relations of $\xi(D)$ given by Eq. (10) with exponents $q > 0$ are mainly included in the analysis to outline the total range of modeled snowfall triple-frequency radar signatures.

In addition to analyzing snowfall triple-frequency radar signatures for synthetically generated $\xi(D)$ relations, first results for using snowflake complexity $\chi$ derived from 2D images as indicator of normalized snowflake surface area-to-volume ratio $\xi$ are also presented in Sect. 4.2. The method relies on the results of fitting $\chi(D)$ relations following Eq. (2) to the MASC data in Fig. 3. To determine $\xi$ values from the fitted $\chi(D)$ relations, it is assumed that the snowflake complexity range of $1 \leq \chi(D) \leq \chi(D_{\max}) = \chi_{\max}$ corresponds to the full snowflake SAV range of $1 \leq \xi \leq 5$, and the derived range of $\chi(D)$ values is rescaled to the full range of $\xi$ values by

$$\xi(\chi) = 1 + \frac{5-1}{\chi_{\max} - 1}(\chi(D) - 1) . \tag{11}$$

After inserting Eq. (2) for $\chi(D)$, Eq. (11) again leads to a modified power law for $\xi(D)$ given by Eq. (10), with power-law exponent of $q = b$. Only the scaling factor $a$ in Eq. (2) is modified by Eq. (11) to confine $\xi(\chi)$ to the interval of $1 \leq \xi \leq 5$.

High values of $q \gg 1$ in Eq. (10) lead to $\xi(D)$ relations marked by a steep increase from $\xi = 1$ to $\xi = 5$ for large snowflake diameters (see Fig. 5), corresponding to a sudden change in snowflake shape from ice spheres to complex 3D shapes found for aggregates, for example. This is an unrealistic description of snowflake shape because such an abrupt transition is not seen in

**12**

snowflake observations. Figure 3 showed power-law exponents of $b \lesssim 1$, leading to $q \lesssim 1$ according to Eq. (11). Nonetheless, $\xi(D)$ with $q \gg 1$ are also included for completeness. Section 4.2 indicates that these $\xi(D)$ relations only contribute a small fraction to the total range of modeled snowfall triple-frequency radar signatures and are not crucial to the drawn conclusions.

To determine radar reflectivity factors $Z_e$ with Eq. (8), backscatter cross sections $\sigma_{\mathrm{b}}(D;\xi)$ for collections of multiple ice
5   spheres are only calculated for snowflake diameters of $D > 0.55$ mm, corresponding to mass-equivalent ice sphere radii of $r_{\mathrm{eq}} > 0.16$ mm. For smaller snowflakes, Eq. (3) leads to high snowflake densities that cannot be reached consistently by randomly distributing non-overlapping ice spheres inside the snowflake bounding volume. Here, $\sigma_{\mathrm{b}}$ is only calculated for a single mass-equivalent ice sphere specified by $\xi = 1$, and the value of $\sigma_{\mathrm{b}}(D;\xi = 1)$ is then assigned to all ice sphere collections, leading to $\sigma_{\mathrm{b}}(D; 1 \leq \xi \leq 5) = \sigma_{\mathrm{b}}(D;\xi = 1)$ for $D \leq 0.55$ mm or $r_{\mathrm{eq}} \leq 0.16$ mm. This simplification has no significant impact on
10   modeled triple-frequency radar signatures in Sect. 4.2 because snowfall radar reflectivity factors determined from Eq. (8) are only affected weakly by the backscatter cross sections of small snowflakes. Even when snowflake diameters of $D \leq 0.55$ mm are ignored completely, modeled $Z_e$ and DWRs decrease by less than 0.3 dB for snowflake size distributions with exponential slope parameters of $\Lambda \leq 2.0$ mm$^{-1}$. Slightly higher changes in modeled $Z_e$ and DWRs are found for snowflake size distributions characterized by higher values of $\Lambda$, with maximum differences of 1.7 dB in modeled $Z_e$ at 94 GHz and 0.8 dB in derived
15   DWR Ka/W for an extreme slope parameter of $\Lambda = 5.0$ mm$^{-1}$. These differences are generally much smaller than the impact of snowflake SAV on modeled $Z_e$ and DWRs in Sect. 4.2.

At 10 and 14 GHz, all $\sigma_{\mathrm{b}}(D; 1 < \xi \leq 5)$ for $0.55 < D \leq 1.4$ mm or $0.16 < r_{\mathrm{eq}} \leq 0.3$ mm are additionally replaced by $\sigma_{\mathrm{b}}(D;\xi = 1)$ to obtain smooth spline interpolants of $\sigma_{\mathrm{b}}(D; 1 \leq \xi \leq 5)$ in Sect. 4.1. The effect of these modifications on modeled triple-frequency radar signatures in Sect. 4.2 is negligible, with associated differences in modeled $Z_e$ and in DWR X/Ka
20   and DWR Ku/Ka of less than 0.1 dB for all analyzed snowflake size distributions.

## 4   Modeling results and discussion

### 4.1   Snowflake backscatter cross sections

Figure 6 presents snowflake backscatter cross sections $\sigma_{\mathrm{b}}$ modeled according to Sect. 3.2 at 35 and 94 GHz and for snowflake diameters of $D \leq 14.4$ mm, corresponding to mass-equivalent ice sphere radii of $r_{\mathrm{eq}} \leq 1.5$ mm. The total range of $\sigma_{\mathrm{b}}$ for all
25   diameters of $D \leq 23.6$ mm, for all considered snowflake approximations, and for frequencies of 10 and 14 GHz is included in Fig. S3 in the Supplement.

For soft spheres, Figs. 6 and S3 show strong resonances in calculated $\sigma_{\mathrm{b}}$ typical for applying Mie scattering theory to large particles (Mie, 1908; Bohren and Huffman, 1983). The higher the frequency, and thus the larger the effective size of a spherical particle with diameter $D$ relative to the wavelength, the more oscillations are observed within the total diameter range.
30   Oscillations in $\sigma_{\mathrm{b}}$ are heavily dampened for spheroids due to orientation averaging of $\sigma_{\mathrm{b}}$ to reflect random snowflake orientation and for SSRGA results due to averaging over an ensemble of many different realizations of non-spherical snowflake shape models. Collections of randomly distributed (solid) ice spheres also lead to much weaker oscillations in $\sigma_{\mathrm{b}}$ than soft spheres of diameter $D$ because calculated $\sigma_{\mathrm{b}}(D;\xi)$ are determined as ensemble averages of 500 realizations for each configuration of
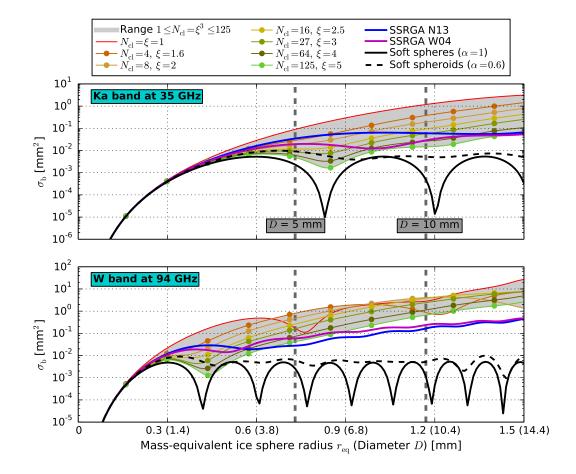
**Figure 6.** Modeled snowflake backscatter cross sections $\sigma_{\mathrm{b}}$ at 35 and 94 GHz for (i) collections of randomly distributed ice spheres of $1 \leq N_{\mathrm{cl}} \leq 125$ constituent ice spheres, corresponding to normalized surface area-to-volume ratios of $1 \leq \xi \leq 5$, for (ii) the self-similar Rayleigh-Gans approximation (SSRGA) applied to N13 and to W04 snowflake 3D shape models, and for (iii) soft spheres and oblate spheroids with aspect ratios of $\alpha = 1$ and $\alpha = 0.6$, respectively. Results for (single) mass-equivalent ice spheres given by $N_{\mathrm{cl}} = 1$, for snowflakes modeled according to the SSRGA, and for soft ice spheres and spheroids were calculated at a resolution of $\Delta r_{\mathrm{eq}} = 0.01$ mm. For ice sphere collections with $N_{\mathrm{cl}} = 4$, 8, 16, 27, 64, and 125, dots mark values of $\sigma_{\mathrm{b}}(D; \xi)$ that were calculated at a resolution of $\Delta r_{\mathrm{eq}} \approx 0.14$ mm following Sect. 3.2, and lines indicate spline interpolations of the calculated $\sigma_{\mathrm{b}}(D; \xi)$. Modeled $\sigma_{\mathrm{b}}$ for the full range of considered snowflake diameters $D \leq 23.6$ mm, for soft spheroids characterized by extreme aspect ratios of $\alpha = 0.2$, and for microwave frequencies of 10 and 14 GHz are shown in Fig. S3 in the Supplement.

$N_{\mathrm{cl}} = \xi^3 > 1$ and because the individual ice spheres are characterized by a radius of $r_{\mathrm{cl}} \ll D/2$, and thus by a much smaller effective size relative to the wavelength (see Sect. 3.2).

In Fig. 6, calculated backscatter cross sections $\sigma_{\mathrm{b}}(D; \xi)$ for collections of randomly distributed ice spheres of $1 \leq N_{\mathrm{cl}} = \xi^3 \leq 125$ constituent ice spheres alone cover a maximum range of over 2 orders of magnitude for $r_{\mathrm{eq}} \approx 0.85$ mm or $D \approx 6.3$ mm

at 35 GHz and for $r_{\mathrm{eq}} \approx 0.44$ mm or $D \approx 2.4$ mm at 94 GHz. Outside the Mie resonance regions, $\sigma_{\mathrm{b}}(D;\xi)$ decrease with increasing normalized snowflake surface area-to-volume ratio $\xi$. This trend is consistent with results of Honeyager et al. (2014) who found smaller backscatter cross sections for greater snowflake surface complexity when modeling microwave backscatter for detailed snowflake 3D shape models with the discrete dipole approximation.

A comparison of the $\sigma_{\mathrm{b}}$ curves in Figs. 6 and S3 shows that differences in $\sigma_{\mathrm{b}}$ associated with the choice of snowflake approximation generally increase with increasing snowflake diameter and microwave frequency. In Fig. 6, $\sigma_{\mathrm{b}}$ curves can only be distinguished visibly from each other for $r_{\mathrm{eq}} > 0.3$ mm or $D > 1.4$ mm at 35 GHz while $\sigma_{\mathrm{b}}$ curves already split for $r_{\mathrm{eq}} \approx 0.2$ mm or $D \approx 0.6$ mm at 94 GHz, for example. SSRGA results for the N13 and W04 snowflake parameterizations are similar to each other and fall within the range of modeled $\sigma_{\mathrm{b}}(D;\xi)$ for collections of randomly distributed ice spheres with $1 \leq N_{\mathrm{cl}} = \xi^3 \leq 125$ for small snowflake diameters and low microwave frequencies. For large snowflake diameters and high frequencies, however, backscatter cross sections $\sigma_{\mathrm{b}}$ calculated by the SSRGA are up to 1 order of magnitude smaller than the minimum $\sigma_{\mathrm{b}}(D;\xi)$. Compared to soft spheres, $\sigma_{\mathrm{b}}$ values calculated by the SSRGA are up to 4 orders of magnitude higher.

The N13 and W04 snowflake parameterizations according to the SSRGA that are used in this study were originally derived for snowflake 3D shape models with diameters $D \lesssim 10$ mm by Hogan et al. (2017). Nonetheless, these SSRGA parameterizations are applied to snowflake diameters up to $D_{\mathrm{max}} = 23.6$ mm in the presented analysis to allow a direct comparison with modeled backscatter by collections of randomly distributed ice spheres and by soft spheres and spheroids (briefly discussed below).

Vertical dashed lines in Figs. 6 and S3 indicate diameters of $D = 5.0$ mm and $D = 10.0$ mm used as maximum diameters $D_{\mathrm{max}}$ for the analysis of truncated snowflake size distributions in Sect. 4.2. Combined with the analysis of modeled snowfall triple-frequency radar signatures for $D_{\mathrm{max}} = 23.6$ mm, the results for truncated snowflake size distributions at $D_{\mathrm{max}} = 10.0$ mm and at $D_{\mathrm{max}} = 5.0$ mm then characterize the impact of large snowflakes with $D > 10.0$ mm and with $D > 5.0$ mm on modeled snowfall triple-frequency radar signatures.

Notably, snowfall triple-frequency radar signatures modeled according to the SSRGA for N13 and W04 snowflake parameterizations and truncated snowflake size distributions at $D_{\mathrm{max}} = 10.0$ mm in Sect. 4.2 show similar characteristic differences with respect to triple-frequency radar signatures modeled for collections of randomly distributed ice spheres and for soft spheres and spheroids as the differences found for snowflake size distributions spanning the total analyzed range of diameters up to $D_{\mathrm{max}} = 23.6$ mm. Therefore, application of the two SSRGA snowflake parameterizations beyond the size range they were originally derived for by Hogan et al. (2017) is not expected to significantly affect the corresponding analysis results and conclusions in this study.

## 4.2 Snowfall triple-frequency radar signatures

An overview of the snowfall radar reflectivity factors $Z_e$ derived from the modeled snowflake backscatter cross sections in Sect. 4.1 are included in Fig. S4 in the Supplement but not discussed in this study. Snowfall triple-frequency radar signatures are shown in Fig. 7. For all considered snowflake models, using DWR Ku/Ka to quantify triple-frequency radar signatures in combination with DWR Ka/W leads to compressed triple-frequency curves by $\Delta$DWR $\lesssim 3$ dB compared to using DWR X/Ka.
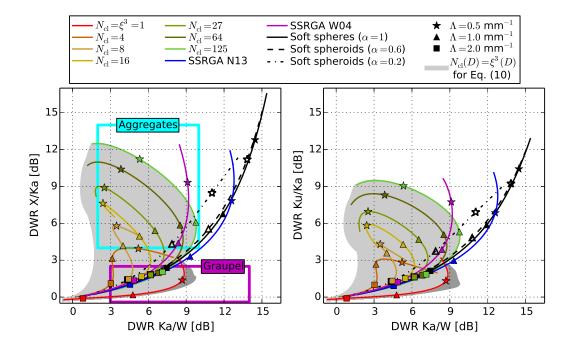
**Figure 7.** Modeled snowfall triple-frequency radar signatures given by dual-wavelength ratios of DWR Ka/W and either DWR X/Ka or DWR Ku/Ka. DWRs are determined according to Sect. 3.3 for exponential size distributions characterized by snowflake diameters of $D \leq 23.6$ mm and by exponential slope parameters of $0.3 \leq \Lambda \leq 5.0$ mm$^{-1}$. Snowflakes are approximated by (i) collections of randomly distributed ice spheres, by (ii) the self-similar Rayleigh-Gans approximation (SSRGA) applied to N13 and to W04 snowflake 3D shape models, and by (iii) soft spheres and oblate spheroids. The gray area indicates the plume of all triple-frequency curves derived for collections of randomly distributed ice spheres that are described by synthetically generated $\xi(D)$ relations expressed through Eq. (10) and summarized in Fig. 5. Darker shade of gray marks the region of DWR combinations that are only derived for high power-law exponents of $q > 2.5$ in Eq. (10). Colored rectangles are adapted from Kneifel et al. (2015) and roughly outline regions associated with the presence of large aggregate snowflakes (cyan) and rimed snowflakes (graupel; magenta) that were derived by relating snowfall triple-frequency radar reflectivity measurements at X, Ka, and W band to coincident in situ snowflake observations. Corresponding triple-frequency radar signatures for snowflake size distributions limited to $D \leq 10.0$ mm and to $D \leq 5.0$ mm are shown in Figs. S5 and S6, respectively.

But the general shape of each curve and characteristic differences among the shapes of all curves are not affected by the choice of defining triple-frequency radar signatures with respect to either DWR X/Ka or DWR Ku/Ka.

Triple-frequency curves for soft spheres and spheroids with aspect ratios of $\alpha = 1$, 0.6, and 0.2 in Fig. 7 are characterized by strictly increasing DWRs with decreasing exponential slope parameters $\Lambda$ of the snowflake size distribution. For a given value of $\Lambda$, DWRs determined for the three aspect ratios are generally within 3 dB from each other, except for very broad size distributions with $\Lambda \leq 0.5$ mm$^{-1}$.

Modeled triple-frequency radar signatures for the N13 and W04 snowflake parameterizations according to the SSRGA roughly follow the shape of the curves determined for spheroidal snowflake approximations for high values of $\Lambda$, but show

a maximum in DWR Ka/W near $\Lambda \approx 0.5$ mm$^{-1}$. A further decrease of $0.5 \geq \Lambda \geq 0.3$ mm$^{-1}$ then leads to a decrease in DWR Ka/W by less than 1 dB, resulting in triple-frequency curves roughly shaped like a comma sign.

The shapes of triple-frequency curves derived for collections of randomly distributed ice spheres inside the snowflake bounding volume and shown in Fig. 7 are markedly different from the triple-frequency curves derived for soft spheres and spheroids

5 and for the N13 and W04 snowflake parameterizations according to the SSRGA. Curves derived for low normalized surface area-to-volume ratios of $\xi \approx 1$ only show a slow increase in DWR X/Ka or DWR Ku/Ka with decreasing $\Lambda$ and therefore occupy a region below the triple-frequency curves determined for soft spheres and spheroids and for the N13 and W04 snowflake parameterizations. Increasing values of $\xi$ lead to curves that follow the shapes of the triple-frequency curves derived for soft spheres and spheroids with $\alpha = 1$ and $\alpha = 0.6$ for narrow snowflake size distributions characterized by high values of $\Lambda$.

10 However, triple-frequency curves derived for randomly distributed ice spheres generally reach a strong local maximum of DWR Ka/W at an intermediate value of $\Lambda$ and then sharply bend back toward lower DWR Ka/W with a further decrease in $\Lambda$. This behavior leads to hook-shaped triple-frequency curves. The strength of the 'hooking' increases with increasing surface area-to-volume ratio, quantified by the difference between maximum DWR Ka/W and the value of DWR Ka/W that corresponds to the minimum slope parameter of $\Lambda = 0.3$ mm$^{-1}$. Additionally, higher values of $\xi$ result in triple-frequency curves

15 that roughly follow the shape of spheroidal curves up to higher values of DWR X/Ka or DWR Ku/Ka before hooking toward lower DWR Ka/W (see also Fig. 8 for triple-frequency curves determined for $\xi = 6$).

Modeling snowfall triple-frequency radar signatures for collections of randomly distributed ice spheres inside the snowflake bounding volume leads to a much wider range of triple-frequency radar signatures in Fig. 7 than the region between the triple-frequency curves that were derived for soft spheres and spheroids or for the N13 and W04 snowflake parameterizations

20 according to the SSRGA. Modeled triple-frequency curves for $1 \leq \xi \leq 5$ cover a range of up to about 7 dB for DWR Ka/W at $\Lambda = 1.0$ mm$^{-1}$, 10 dB for DWR X/Ka at $\Lambda = 0.5$ mm$^{-1}$, and 8 dB for DWR Ku/Ka at $\Lambda = 0.5$ mm$^{-1}$. In contrast, soft spheres and spheroids or the N13 and W04 snowflake parameterizations according to the SSRGA only show corresponding DWR ranges of about 3 dB and less.

The total range of triple-frequency radar signatures modeled for collections of randomly distributed ice spheres in Fig. 7

25 covers a large part of all observed triple-frequency signatures in snowfall radar reflectivity measurements by Kulie et al. (2014), Kneifel et al. (2015), and Yin et al. (2017). Additionally, modeled triple-frequency radar signatures for intermediate and high values of $\xi$ combined with small $\Lambda$ correspond to triple-frequency radar signatures that were related to the presence of large aggregate snowflakes by Kneifel et al. (2015). The region of triple-frequency radar signatures that they related to snowfall characterized by rimed snowflakes (denoted as graupel in Fig. 7) contains modeled triple-frequency curves for low surface

30 area-to-volume ratios given by $\xi \approx 1$ in this study. High values of $\xi$ indicate high snowflake surface area-to-volume ratios, and thus a high complexity of the snowflake microstructure (Sect. 3.2), as expected for aggregate snowflakes. Furthermore, broad snowflake size distributions characterized by small $\Lambda$ in Eq. (1) contain a higher amount of large snowflakes, consistent with the observation of large aggregates for triple-frequency radar signatures that correspond to small $\Lambda$. Snowflake riming, on the other hand, is associated with a rounding of the snowflake microstructure due to the aggregation of supercooled water droplets. This

35 reduction in the complexity of the snowflake microstructure for rimed snowflakes is reflected in the applied modeling approach

Atmospheric
Chemistry
and Physics
Discussions

Open Access

by low normalized snowflake surface area-to-volume ratios of $\xi \approx 1$ (Sect. 3.2), leading to relatively flat triple-frequency curves for graupel snow. In sharp contrast, triple-frequency curves determined for soft spheres and spheroids and for the N13 and W04 snowflake parameterizations according to the SSRGA only cover a much smaller region of the indicated range of observed snowfall triple-frequency radar signatures and cannot explain the distinct regions related to the presence of large aggregates

5 and rimed snowflakes in Fig. 7. Notably, even if various combinations of snowflake gamma size distributions, density-diameter relations, aspect ratios, and orientation angles are used to model snowfall triple-frequency radar signatures for soft spheroids, the range of modeled triple-frequency radar signatures does not show a significantly better agreement with the observed range of snowfall triple-frequency signatures in radar reflectivity measurements (e.g., Leinonen et al., 2012; Kneifel et al., 2015).

The hook shape of triple-frequency curves derived for intermediate and high values of $\xi$ in Fig. 7 is similar to the characteris-

10 tic shape of snowfall triple-frequency radar signatures that were previously modeled by Kneifel et al. (2011) and Leinonen et al. (2012) based on detailed 3D approximations of non-spheroidal snowflake shape models. Neither soft spheres and spheroids nor the N13 and W04 snowflake parameterizations according to the SSRGA yield triple-frequency curves showing this characteristic behavior with a strong maximum of DWR Ka/W at intermediate values of $\Lambda$.

Comparing radar reflectivity measurements and in situ snowflake observations, Kneifel et al. (2015) also found that a clear

15 distinction between different snow types was not possible for combinations of low DWR Ka/W and low DWR X/Ka. Within the modeling approach presented in this study, this ambiguity can be explained by the similarity of all triple-frequency curves in Fig. 7 that are determined for narrow snowflake size distributions characterized by high values of $\Lambda$. For narrow snowflake size distributions, modeled triple-frequency radar signatures are dominated by small snowflakes. Even at 94 GHz, the differences in modeled backscatter cross sections for the total SAV range of $1 \leq \xi \leq 5$ shown in Figs. 6 and S3 are not significant enough

20 for small snowflakes to cause a clear separation of the triple-frequency curves for high $\Lambda$ in Fig. 7. For larger snowflakes, larger differences among modeled snowflake backscatter cross sections are observed in Figs. 6 and S3. Broader snowflake size distributions characterized by lower values of $\Lambda$ contain a higher amount of large snowflakes and therefore lead to more easily distinguishable triple-frequency curves in Fig. 7.

Modeled snowfall triple-frequency radar signatures for the MASC measurements of snowflake complexity that were pre-

25 sented in Sect. 2.2 are shown in Fig. 8. The derived $\xi(D)$ relations according to Eqs. (2) and (11) still lead to characteristic hook-shaped triple-frequency curves with a local maximum of DWR Ka/W observed at intermediate values of $\Lambda$. However, the maximum of DWR Ka/W is already found at lower values of DWR Ka/W and is therefore less pronounced than for triple-frequency curves derived for constant normalized snowflake surface area-to-volume ratios of $\xi \gtrsim 3$ in Fig. 7.

Thus far, all snowfall radar signatures have been determined for exponential snowflake size distributions with snowflake

30 diameters of $D \leq D_{\mathrm{max}} = 23.6$ mm. To investigate the impact of truncating snowflake size distributions already at smaller maximum diameters, snowfall triple-frequency radar signatures were also modeled for exponential snowflake size distributions limited to $D \leq D_{\mathrm{max}} = 10.0$ mm and $D \leq D_{\mathrm{max}} = 5.0$ mm. The modeling results are presented in Figs. S5 and S6 in the Supplement and summarized in Fig. 9. In general, truncation at smaller $D_{\mathrm{max}}$ leads to an 'un-hooking' or flattening of the derived triple-frequency curves. For $D \leq 10.0$ mm, modeled snowfall triple-frequency radar signatures in Fig. 9 follow the

35 corresponding triple-frequency curves derived for $D \leq 23.6$ mm down to snowflake size distributions characterized by expo-
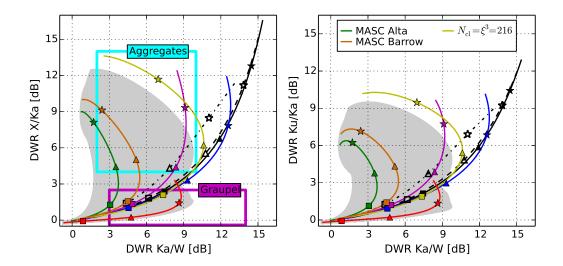
**Figure 8.** Modeled snowfall triple-frequency radar signatures for exponential size distributions with snowflake diameters of $D \leq 23.6$ mm. The notation follows Fig. 7 with additional DWRs calculated for a constant normalized surface area-to-volume ratio of $\xi = 6$ and by applying Eq. (11) to the MASC measurement results shown in Fig. 3. Corresponding triple-frequency radar signatures for exponential size distributions limited to $D \leq 10.0$ mm are presented in Fig. S7.

nential slope parameters of $\Lambda \approx 1.0$ mm$^{-1}$, before splitting off toward higher values of DWR Ka/W. Triple-frequency curves derived for $D \leq 5.0$ mm already start to deviate visibly from the two corresponding curves determined for $D \leq 23.6$ mm and for $D \leq 10.0$ mm at higher values of $\Lambda \approx 2.0$ mm$^{-1}$. Additionally, truncating snowflake size distributions at $D_{\max} = 5.0$ mm leads to a smaller total range of modeled DWR X/Ka and DWR Ku/Ka, and for low normalized surface area-to-volume ratios,

5    indicated by $N_{\mathrm{cl}} = \xi = 1$ in Fig. 9, also to a smaller total range of modeled DWR Ka/W.

For snowflake size distributions limited to diameters of $D \leq D_{\max} = 10.0$ mm, snowfall triple-frequency radar signatures determined from MASC measurements of snowflake complexity $\chi$ are shown in Figure S7. Compared to Fig. 8, truncation at $D_{\max} = 10.0$ mm leads to an increase in modeled DWRs of up to about 3 dB. These differences are caused by the strong impact of $D_{\max}$ on the value of $\chi(D_{\max}) = \chi_{\max}$ calculated with Eq. (2), which translates to higher normalized snowflake

10    surface area-to-volume ratios $\xi(\chi)$ for $D \leq D_{\max} = 10.0$ mm following Eq. (11). A reliable determination of $D_{\max}$ for the analyzed snowflake size distributions is therefore crucial for deriving snowflake surface area-to-volume ratios from snowflake complexity measurements and then modeling snowfall triple-frequency radar signatures.

Combining the characteristic hook shape of triple-frequency curves derived for high surface area-to-volume ratios in Figs. 7 and 8 with the flattening of triple-frequency curves due to the truncation of snowflake size distributions at smaller maximum

15    diameters as illustrated in Fig. 9, modeled triple-frequency radar signatures for snowfall characterized by high snowflake surface area-to-volume ratios and small snowflake diameters can resemble snowfall triple-frequency radar signatures modeled for soft spheroids. This explains why some non-spheroidal snowflake shape models may lead to similarly high val-
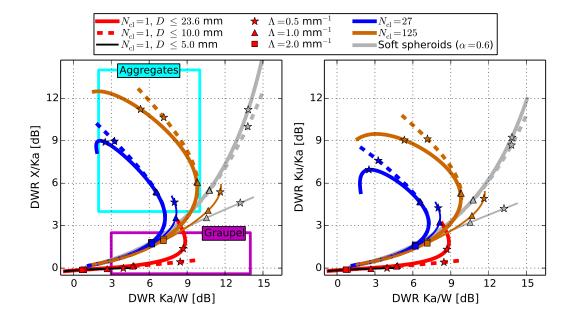
**Figure 9.** Impact of snowflake maximum diameter $D_{\mathrm{max}} = 23.6$, 10.0, 5.0 mm on modeled snowfall triple-frequency radar signatures for exponential snowflake size distributions with exponential slope parameters of $0.3 \leq \Lambda \leq 5.0$ mm$^{-1}$. Modeling results for snowflakes approximated as collections of $N_{\mathrm{cl}} = 1$, 27, 125 randomly distributed ice spheres inside the bounding volume correspond to normalized snowflake surface area-to-volume ratios of $\xi = 1$, 3, 5, respectively.

ues of modeled DWR Ka/W $> 10$ dB as soft spheroids, e.g., for the aggregates of needle-shaped ice crystals analyzed by Leinonen et al. (2012). According to Fig. 9, values of DWR Ka/W $> 10$ dB are expected for snowfall characterized by normalized snowflake surface area-to-volume ratios of $\xi \approx 5$ and exponential snowflake size distributions limited to snowflake diameters of $D \leq D_{\mathrm{max}} = 5.0$ mm with exponential slope parameters of $\Lambda \lesssim 1$ mm$^{-1}$. Even higher values of $\xi > 5$ already

5   lead to similarly high values of DWR Ka/W for less restrictive snowflake size distributions with respect to $D_{\mathrm{max}}$ and $\Lambda$.

　　All presented results have been determined for only one parameterization of snowflake mass $m_{\mathrm{f}}(D)$ according to Sect. 3.1. Previous studies have shown, however, that the uncertainty in modeled snowfall radar reflectivity factors $Z_e$ due to the parameterization of $m_{\mathrm{f}}(D)$ is significant. Hammonds et al. (2014) found uncertainties in $Z_e$ related to $m_{\mathrm{f}}(D)$ on the order of 4 dB at X, Ku, Ka, and W band, for example. To evaluate the impact of the parameterization of snowflake mass on the modeled snowfall

10   triple-frequency radar signatures in this study, DWRs for low, intermediate, and high normalized surface area-to-volume ratios of $\xi = 1$, 3, 5 were also derived after modifying the density values $\rho_{\mathrm{f}}(D)$ obtained from the H04 density-diameter relation in Eq. (3) by $\pm 25\,\%$ and $\pm 50\,\%$. Derived triple-frequency curves for the modified relations of $\rho_{\mathrm{f}}(D)$ are presented in Figs. S8 and S9, and the impact of $\rho_{\mathrm{f}}(D)$ on modeled $Z_e$ and DWRs is summarized in Fig. 10.

　　Figure 10 shows that the analyzed $\rho_{\mathrm{f}}(D)$ range leads to a corresponding range in modeled $Z_e$ of $\Delta\mathrm{dB}Z_e > 3.5$ dB and a

15   range in derived DWRs of $\Delta\mathrm{DWR} < 3.0$ dB. Generally, differences of $\Delta\mathrm{dB}Z_e \gtrsim 6$ dB and of $\Delta\mathrm{DWR} \lesssim 1$ dB are found, except
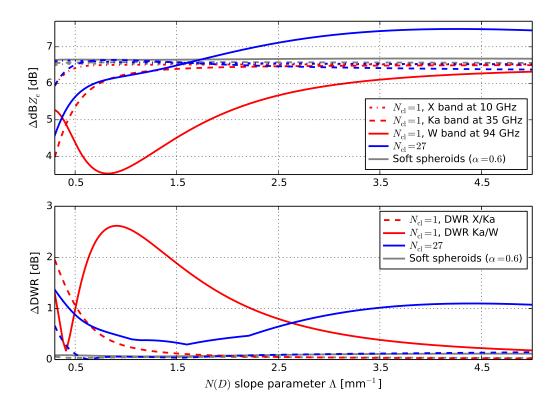
**Figure 10.** Impact of snowflake density $\rho_{\mathrm{f}}(D)$ on modeled snowfall radar reflectivity factors $Z_e$ and dual-wavelength ratios (DWRs) for exponential size distributions with snowflake diameters of $D \leq 23.6$ mm and exponential slope parameters of $0.3 \leq \Lambda \leq 5.0$ mm$^{-1}$. Shown $\Delta\mathrm{dB}Z_e$ and $\Delta$DWR curves indicate the maximum difference in derived dB$Z_e$ values and DWRs that is associated with the total analyzed $\rho_{\mathrm{f}}(D)$ range given by modifying all $\rho_{\mathrm{f}}(D)$ determined from Eq. (3) by $\pm25\,\%$ and $\pm50\,\%$. Modeling results for dB$Z_e$ at 14 GHz and for DWR Ku/Ka are similar to shown dB$Z_e$ at 10 GHz and DWR X/Ka, respectively. Collections of randomly distributed ice spheres with a surface area-to-volume ratio given by $\xi = 5$ or $N_{\mathrm{cl}} = 125$ lead to similar $\Delta\mathrm{dB}Z_e$ and $\Delta$DWR as the included ice sphere collections with $N_{\mathrm{cl}} = 27$ or $\xi = 3$.

for snowfall characterized by $\xi = 1$, indicative of heavily rimed graupel snow, and snowflake size distributions with exponential slope parameters of $\Lambda \lesssim 2$ mm$^{-1}$. Similar trends are also observed for snowflake size distributions limited to $D \leq 10.0$ mm and $D \leq 5.0$ mm (not shown). These results indicate that modeled DWRs are less sensitive to uncertainties associated with the parameterization of snowflake mass than modeled $Z_e$ at a single wavelength.

5    Even high differences of $\Delta$DWR $> 1$ dB associated with changes in $\rho_{\mathrm{f}}(D)$ of up to $\pm50\,\%$ are still smaller than differences in DWR Ka/W, DWR X/Ka, and DWR Ku/Ka that are associated with the range of normalized surface area-to-volume ratios of $1 \leq \xi \leq 5$ and illustrated in Figs. 7 and 8. The presented analysis then suggests that a realistic characterization of snowflake surface area-to-volume ratio is crucial for a quantitative interpretation of observed and modeled snowfall triple-frequency radar signatures.

Atmospheric
Chemistry
and Physics
Discussions

# 5 Conclusions

In this study, snowflake (radar) backscatter cross sections were modeled at X-, Ku-, Ka-, and W-band radar frequencies of 10, 14, 35, and 94 GHz by approximating each snowflake as a collection of randomly distributed ice spheres. The number and size of the constituent ice spheres are defined by the snowflake mass derived from the snowflake maximum dimension $D$ and by the snowflake ice surface area-to-volume ratio (SAV); the bounding volume of each collection of ice spheres is given by a sphere of diameter $D$. SAV was quantified through the normalized ratio $\xi$ of snowflake SAV to the SAV of a single mass-equivalent solid ice sphere.

Snowfall triple-frequency radar signatures were then determined from dual-wavelength ratios (DWRs) of the snowfall equivalent radar reflectivity factors $Z_e$ that were calculated using the modeled snowflake backscatter cross sections. Based on observational data collected by high-resolution snowflake imaging, $Z_e$ and DWRs were calculated for exponential snowflake size distributions with snowflake diameters of $D \leq D_{\max} = 23.6$ mm and exponential slope parameters of $0.3 \leq \Lambda \leq 5.0$ mm$^{-1}$.

The analysis focused on the impact of snowflake surface area-to-volume ratio on modeled snowfall triple-frequency radar signatures. Additionally, first results were shown for determining snowfall triple-frequency radar signatures from snowflake complexity values that were derived from snowflake images and averaged over one winter season. Finally, the effect of truncating snowflake size distributions at $D_{\max} = 10.0$ mm and at $D_{\max} = 5.0$ mm on modeled triple-frequency radar signatures was investigated, and the impact of the parameterization of snowflake mass on derived DWRs was evaluated by increasing and decreasing all snowflake densities by up to 50 %.

Important results and conclusions are summarized by the following bullet points:

– Average snowflake complexity increases with increasing snowflake size.

– Snowflake complexity values obtained via high-resolution multi-view imaging may be used as indicator of snowflake surface area-to-volume ratio (SAV).

– Modeled snowflake backscatter cross sections generally decrease with increasing SAV.

– Modeled snowfall triple-frequency radar signatures cover a wide range of snowfall triple-frequency signatures previously determined from radar reflectivity measurements.

– Snowflake SAV and truncated snowflake size distributions offer a physical interpretation of snowfall triple-frequency radar signatures that is consistent with previously observed differences in snowfall triple-frequency radar signatures related to the presence of large aggregate snowflakes and rimed snowflakes and that explains why some snowfall triple-frequency radar signatures apparently point to a spheroidal snowflake shape.

– While modeled $Z_e$ show high sensitivity to the parameterization of snowflake mass, with typical differences of $\Delta \mathrm{dB} Z_e \gtrsim 6$ dB for the analyzed snowflake density range, derived DWRs are less sensitive, with corresponding differences of $\Delta \mathrm{DWR} \lesssim 1$ dB except for low SAV.

Atmospheric
Chemistry
and Physics
Discussions

– The analyzed impact of the parameterization of snowflake mass on modeled snowfall triple-frequency radar signatures is generally much smaller than the impact of snowflake SAV.

The results and conclusions suggest two avenues for further research:

1. It would be interesting to adapt the outlined approach for deriving normalized snowflake surface area-to-volume ratio $\xi$ from snowflake images to individual snowstorms and thus obtain snowstorm-specific $\xi(D)$ relations. Snowfall triple-frequency radar signatures could then be modeled for individual snowstorms, following the modeling method presented in this study or a similar approach that accounts for snowflake surface area-to-volume ratio, and compared to coincident triple-frequency radar reflectivity measurements.

2. The strong impact of snowflake surface area-to-volume ratio on modeled snowfall triple-frequency radar signatures indicates that current and future databases of microwave scattering properties determined for detailed snowflake 3D shape models would benefit from including snowflake surface area as additional microstructural parameter (besides snowflake size and density, mass, or ice volume). Differences in modeled scattering properties due to the snowflake shape could then be related not only to visually distinct snow types, identified by characteristic geometric shapes resembling the snowflake microstructure, but also to snowflake surface area-to-volume ratio, providing a quantitative description of the snowflake microstructure across all snow types.

## 6   Data availability

Modeled snowflake backscatter cross sections and derived dual-wavelength ratios of snowfall equivalent radar reflectivity factors are included in the Supplement. Additional data may be obtained by contacting the corresponding author.

*Competing interests.*  T. J. Garrett is a member of the editorial board of the journal and has a financial interest in Particle Flux Analytics which sells the MASC.

Atmospheric
Chemistry
and Physics
Discussions

# References

Bohren, C. F. and Huffman, D. R.: Absorption and scattering of light by small particles, ISBN 0-471-05772-X, John Wiley & Sons, Inc., 1983.

Brandes, E. A., Ikeda, K., Zhang, G., Schönhuber, M., and Rasmussen, R. M.: A statistical and physical description of hydrometeor distributions in Colorado snowstorms using a video disdrometer, J. Appl. Meteorol. Climatol., 46, 634–650, doi:10.1175/JAM2489.1, 2007.

Draine, B. T. and Flatau, P. J.: Discrete-dipole approximation for scattering calculations, J. Opt. Soc. Am. A, 11, 1491–1499, doi:10.1364/JOSAA.11.001491, 1994.

Fontaine, E., Schwarzenboeck, A., Delanoë, J., Wobrock, W., Leroy, D., Dupuy, R., Gourbeyre, C., and Protat, A.: Constraining mass-diameter relations from hydrometeor images and cloud radar reflectivities in tropical continental and oceanic convective anvils, Atmos. Chem. Phys., 14, 11 367–11 392, doi:10.5194/acp-14-11367-2014, 2014.

Garrett, T. J. and Yuter, S. E.: Observed influence of riming, temperature, and turbulence on the fallspeed of solid precipitation, Geophys. Res. Lett., 41, 6515–6522, doi:10.1002/2014GL061016, 2014.

Garrett, T. J., Fallgatter, C., Shkurko, K., and Howlett, D.: Fall speed measurement and high-resolution multi-angle photography of hydrometeors in free fall, Atmos. Meas. Tech., 5, 2625–2633, doi:10.5194/amt-5-2625-2012, 2012.

Gergely, M. and Garrett, T. J.: Impact of the natural variability in snowflake diameter, aspect ratio, and orientation on modeled snowfall radar reflectivity, J. Geophys. Res. Atmos., 121, 12 236–12 252, doi:10.1002/2016JD025192, 2016.

Grenfell, T. C. and Warren, S. G.: Representation of a nonspherical ice particle by a collection of independent spheres for scattering and absorption of radiation, J. Geophys. Res., 104, 31,697–31,709, doi:10.1029/1999JD900496, 1999.

Grenfell, T. C., Neshyba, S. P., and Warren, S. G.: Representation of a nonspherical ice particle by a collection of independent spheres for scattering and absorption of radiation: 3. Hollow columns and plates, J. Geophys. Res., 110, D17 203, doi:10.1029/2005JD005811, 2005.

Hammonds, K. D., Mace, G. G., and Matrosov, S. Y.: Characterizing the radar backscatter-cross-section sensitivities of ice-phase hydrometeor size distributions via a simple scaling of the Clausius-Mossotti factor, J. Appl. Meteorol. Climatol., 53, 2761–2774, doi:10.1175/JAMC-D-13-0280.1, 2014.

Heymsfield, A. J., Bansemer, A., Schmitt, C., Twohy, C., and Poellot, M. R.: Effective ice particle densities derived from aircraft data, J. Atmos. Sci., 61, 982–1003, 2004.

Hogan, R. J. and Westbrook, C. D.: Equation for the microwave backscatter cross section of aggregate snowflakes using the self-similar Rayleigh-Gans approximation, J. Atmos. Sci., 71, 3292–3301, doi:10.1175/JAS-D-13-0347.1, 2014.

Hogan, R. J., Mittermaier, M. P., and Illingworth, A. J.: The retrieval of ice water content from radar reflectivity factor and temperature and its use in evaluating a mesoscale model, J. Appl. Meteorol. Climatol., 45, 301–317, 2006.

Hogan, R. J., Tian, L., Brown, P. R. A., Westbrook, C. D., Heymsfield, A. J., and Eastment, J. D.: Radar scattering from ice aggregates using the horizontally aligned oblate spheroid approximation, J. Appl. Meteorol. Climatol., 51, 655–671, doi:10.1175/JAMC-D-11-074.1, 2012.

Hogan, R. J., Honeyager, R., Tyynelä, J., and Kneifel, S.: Calculating the millimetre-wave scattering phase function of snowflakes using the Self-Similar Rayleigh-Gans Approximation, Q. J. R. Meteorol. Soc., 143, 834–844, doi:10.1002/qj.2968, 2017.

Honeyager, R., Liu, G., and Nowell, H.: Modeling snowflakes at microwave frequencies, in: American Meteorological Society 14th Conference on Cloud Physics, http://ams.confex.com/ams/14CLOUD14ATRAD/webprogram/Paper250491.html, 2014.

Honeyager, R., Liu, G., and Nowell, H.: Voronoi diagram-based spheroid model for microwave scattering of complex snow aggregates, J. Quant. Spectrosc. Radiat. Transfer, 170, 28–44, doi:10.1016/j.jqsrt.2015.10.025, 2016.

Kikuchi, K., Kameda, T., Higuchi, K., and Yamashita, A.: A global classification of snow crystals, ice crystals, and solid precipitation based on observations from middle latitudes to polar regions, Atmos. Res., 132–133, 460–472, doi:10.1016/j.atmosres.2013.06.006, 2013.

Kneifel, S., Kulie, M. S., and Bennartz, R.: A triple-frequency approach to retrieve microphysical snowfall parameters, J. Geophys. Res., 116, D11 203, doi:10.1029/2010JD015430, 2011.

5 Kneifel, S., von Lerber, A., Tiira, J., Moisseev, D., Kollias, P., and Leinonen, J.: Observed relations between snowfall microphysics and triple-frequency radar measurements, J. Geophys. Res. Atmos., 120, 6034–6055, doi:10.1002/2015JD023156, 2015.

Kneifel, S., Kollias, P., Battaglia, A., Leinonen, J., Maahn, M., Kalesse, H., and Tridon, F.: First observations of triple-frequency radar Doppler spectra in snowfall: Interpretation and applications, Geophys. Res. Lett., 43, 2225–2233, doi:10.1002/2015GL067618, 2016.

Kokhanovsky, A. A. and Zege, E. P.: Scattering optics of snow, Appl. Opt., 43, 1589–1602, 2004.

10 Korolev, A. and Isaac, G.: Roundness and aspect ratio of particles in ice clouds, J. Atmos. Sci., 60, 1795–1808, 2003.

Kulie, M. S. and Bennartz, R.: Utilizing spaceborne radars to retrieve dry snowfall, J. Appl. Meteorol. Climatol., 48, 2564–2580, doi:10.1175/2009JAMC2193.1, 2009.

Kulie, M. S., Bennartz, R., Greenwald, T. J., Chen, Y., and Weng, F.: Uncertainties in microwave properties of frozen precipitation: implications for remote sensing and data assimilation, J. Atmos. Sci., 67, 3471–3487, doi:10.1175/2010JAS3520.1, 2010.

15 Kulie, M. S., Hiley, M. J., Bennartz, R., Kneifel, S., and Tanelli, S.: Triple-frequency radar reflectivity signatures of snow: Observations and ccomparisons with theoretical ice particle scattering models, J. Appl. Meteorol. Climatol., 53, 1080–1098, doi:10.1175/JAMC-D-13-066.1, 2014.

Leinonen, J.: High-level interface to T-matrix scattering calculations: architecture, capabilities and limitations, Opt. Express, 22, 1655–1660, doi:10.1364/OE.22.001655, 2014.

20 Leinonen, J., Kneifel, S., Moisseev, D., Tyynelä, J., Tanelli, S., and Nousiainen, T.: Evidence of nonspheroidal behavior in millimeter-wavelength radar observations of snowfall, J. Geophys. Res., 117, D18 205, doi:10.1029/2012JD017680, 2012.

Liu, G.: Deriving snow cloud characteristics from CloudSat observations, J. Geophys. Res., 113, D00A09, doi:10.1029/2007JD009766, 2008.

Magono, C. and Lee, C. W.: Meteorological classification of natural snow crystals, J. Fac. Sci., Hokkaido University, 2, 321–365, 1966.

25 Matrosov, S. Y.: Radar reflectivity in snowfall, IEEE Trans. Geosci. Remote Sens., 30, 454–461, doi:10.1109/36.142923, 1992.

Matrosov, S. Y.: Modeling backscatter properties of snowfall at millimeter wavelengths, J. Atmos. Sci., 64, 1727–1736, doi:10.1175/JAS3904.1, 2007.

Matrosov, S. Y., Heymsfield, A. J., and Wang, Z.: Dual-frequency radar ratio of nonsperical atmospheric hydrometeors, Geophys. Res. Lett., 32, L13 816, doi:10.1029/2005GL023210, 2005.

30 Mätzler, C. and Wegmüller, U.: Dielectric properties of fresh-water ice at microwave frequencies, J. Phys. D: Appl. Phys., 20, 1623–1630, 1987.

Maxwell Garnett, J. C.: Colours in metal glasses and in metallic films, Philos. Trans. Roy. Soc., A, 203, 385–420, doi:10.1098/rsta.1904.0024, 1904.

Meissner, T. and Wentz, F. J.: The complex dielectric constant of pure and sea water from microwave satellite observations, IEEE Trans.
35 Geosci. Remote Sens., 42, 1836–1849, doi:10.1109/TGRS.2004.831888, 2004.

Mie, G.: Beiträge zur Optik trüber Medien, speziell kolloidaler Metallösungen, Ann. Phys., 330, 377–445, 1908.

Mishchenko, M. I. and Travis, L. D.: Capabilities and limitations of a current FORTRAN implementation of the T-matrix method for randomly oriented, rotationally symmetric scatterers, J. Quant. Spectrosc. Radiat. Transfer, 60, 309–324, 1998.

Atmospheric
Chemistry
and Physics
Discussions

Nowell, H., Liu, G., and Honeyager, R.: Modeling the microwave single-scattering properties of aggregate snowflakes, J. Geophys. Res. Atmos., 118, 7873–7885, doi:10.1002/jgrd.50620, 2013.

Ohser, J. and Mücklich, F.: Statistical analysis of microstructures in materials science, no. ISBN 0-471-97486-2 in Statistics in practice, John Wiley & Sons, Inc., 2000.

5  Ori, D., Maestri, T., Rizzi, R., Cimini, D., Montopoli, M., and Marzano, F. S.: Scattering properties of modeled complex snowflakes and mixed-phase particles at microwave and millimeter frequencies, J. Geophys. Res. Atmos., 119, 9931–9947, doi:10.1002/2014JD021616, 2014.

Petty, G. W. and Huang, W.: Microwave backscatter and extinction by soft ice spheres and complex snow aggregates, J. Atmos. Sci., 67, 769–787, doi:10.1175/2009JAS3146.1, 2010.

10  Picard, G., Arnaud, L., Domine, F., and Fily, M.: Determining snow specific surface area from near-infrared reflectance measurements: numerical study of the influence of grain shape, Cold Reg. Sci. Technol., 56, 10–17, doi:10.1016/j.coldregions.2008.10.001, 2009.

Tiira, J., Moisseev, D. N., von Lerber, A., Ori, D., Tokay, A., Bliven, L. F., and Petersen, W.: Ensemble mean density and its connection to other microphysical parameters of snow as observed in Southern Finland, Atmos. Meas. Tech., 9, 4825–4841, doi:10.5194/amt-9-4825-201, 2016.

15  Tyynelä, J., Leinonen, J., Moisseev, D., and Nousiainen, T.: Radar backscattering from snowflakes: comparison of fractal, aggregate, and soft spheroid models, J. Atmos. Oceanic Technol., 28, 1365–1372, doi:10.1175/JTECH-D-11-00004.1, 2011.

Waterman, P. C.: Symmety, unitarity, and geometry in electromagnetic scattering, Phys. Rev. D, 3, 825–839, 1971.

Westbrook, C. D., Ball, R. C., Field, P. R., and Heymsfield, A. J.: Universality in snowflake aggregation, Geophys. Res. Lett., 31, L15 104, doi:10.1029/2004GL020363, 2004.

20  Xu, Y.-l.: Electromagnetic scattering by an aggregate of spheres, Appl. Opt., 34, 4573–4588, doi:10.1364/AO.34.004573, 1995.

Xu, Y.-l. and Å. S. Gustafson, B.: A generalized multiparticle Mie solution: further experimental verification, J. Quant. Spectrosc. Radiat. Transfer, 70, 395–419, doi:10.1016/S0022-4073(01)00019-X, 2001.

Yin, M., Liu, G., Honeyager, R., and Turk, F. J.: Observed differences of triple-frequency radar signatures between snowflakes in stratiform and convective clouds, J. Quant. Spectrosc. Radiat. Transfer, 193, 13–20, doi:10.1016/j.jqsrt.2017.02.017, 2017.